

764  
NSG-7043

NASA HQ,

7N-92-CR

114152

p/33

GECORONAL STRUCTURE 3, OPTICALLY  
THIN, DOPPLER BROADENED LINE PROFILES

by

James Bishop\* and Joseph W. Chamberlain

Department of Space Physics and Astronomy

Rice University, Houston, Texas USA

RECEIVED  
A.I.A.A.  
1988 OCT -8 AM 9:35  
T.I.S. LIBRARY

(NASA-CR-182311) GECORONAL STRUCTURE 3,  
OPTICALLY THIN, DOPPLER BROADENED LINE  
PROFILES (Rice Univ.) 33 p

N88-70144

Unclas  
00/92 0114152

\*Current Affiliation: Department of Geophysics and Astronomy, Univ. of  
British Columbia, Vancouver, Canada

## ABSTRACT

Theoretical line profiles, applicable to the analysis of geocoronal  $H_{\alpha}$  profile measurements, are presented for illustrative cases. While retaining a number of simplifications (classical exobase, diffusive equilibrium plasmasphere conditions), distinctive spectral signatures of mechanisms governing the geocorona are isolated. Examining the consequences of solar radiation pressure dynamics is the main point here: this operates to form narrow evaporative profiles via the creation of an extensive quasi-satellite component. Comparison with a simple extension of the earlier analytic theory discloses the influence of an exopause in this regard. The main modifications to evaporative spectral shapes in the geocoronal application, for shadow heights greater than two Earth radii, are predicted to be (i) a blueward "shift" or bias near line center, for look directions parallel to the antisolar axis, generated by loss mechanisms acting over the time of flight of exospheric constituents (e.g., solar ionization), and (ii) an enhanced redward wing at spectral displacements exceeding that defined by the shadow height escape speed, produced by plasmaspheric charge exchange collisions. Implications of these results for recent measurements of geocoronal  $H_{\alpha}$  emissions are briefly discussed.

## 1. INTRODUCTION

Chamberlain [1976] served to point out that careful observations of spectral line profiles might aid in resolving numerous questions regarding the geocorona. The impetus for undertaking the current calculations lies in the geocoronal Balmer- $\alpha$  ( $H_{\alpha}$ ) profile intensity measurements recently reported by Yelle and Roesler [1985] and Kerr et al. [1986]. Several aspects of these observations have seemed puzzling when compared with either the Monte-Carlo results of Tinsley and colleagues [Hodges et al., 1981; Tinsley et al., 1986] or with the analytic theory of Chamberlain [1976]. For example, the interpretation of the narrow line widths near midnight presented by Yelle and Roesler are not easily related to the local speed distributions and derived "temperatures" obtained in the Monte-Carlo simulations noted above, while the distinctive shouldered spectrum functions generated by moderate satellite critical radii in the analytic theory are not in evidence. It is believed that some of the confusion is attributable to uncertainty in just what these profiles reveal about the geocorona. The main purpose of this paper is to indicate the sorts of profiles that can be expected in selected cases and to isolate the cause(s) of the principal spectral features. In view of its fundamental influence on geocoronal structure, signatures deriving from the action of radiation pressure are emphasized. Further, a more comprehensive interpretive framework is suggested as being needed to access both the significance of observed features and the potential reliability of such observations as a technique for monitoring processes near the Earth.

In this study, the lines of sight selected for evaluation are along the Earth-Sun axis; a comparison of the results presented in Bishop [1985] and Bishop and Chamberlain [1986] (hereinafter referred to as GS1 and GS2, respectively) indicates that exospheric quantities at near-axis locations do not

vary noticeably from their axial values, so the profiles presented here are directly comparable to observations made along lines of sight roughly parallel to the Earth-Sun axis. Line profiles have been computed for several shadow heights, with an emphasis on column bases well enough away from the exobase that nonuniformities in exobase density and temperature are not likely to mask profile features arising from radiation pressure dynamics and the plasmasphere interaction. The cases considered involve profiles generated by fluorescent scattering in a simple evaporative exosphere, in an exosphere experiencing ionization by solar emissions, and in exospheres interacting with the spherical and dipolar plasmasphere models of GS2. Radiation pressure is rigorously taken into account in each case. The presentation is in terms of both line profiles and, preferably, spectrum functions as defined in Chamberlain [1976]. Use of the spectrum function permits separation of the rather weak features indicative of plasmaspheric charge exchange collisions and solar ionization from the overriding exponential dependence of the profile on the square of the radial speed.

The simplifications retained in this study are appropriate for the aim of erecting a framework for observational analysis. The exobase source of geocoronal hydrogen atoms is characterized by a constant density  $N_c$  and temperature  $T_c$ . Single scattering without shadow region contamination is assumed, tantamount to taking the base of the illuminated region to be a sharp boundary. The incident solar Lyman- $\beta$  flux is not considered to be attenuated by passage through the dayside and terminator regions. Complete frequency redistribution in the fluorescence process is assumed. Profile distortions associated with atomic fine structure are not considered.

## 2. SPECTRUM FUNCTION FORMULATION

The Doppler broadened, optically thin line profile, expressed as an apparent emission rate  $I$ , is (using the dimensionless variables of GS1)

$$4\pi I(\xi, \lambda_1) = g_H K \int_{\lambda} \int_{\zeta} \int_{\epsilon} f \frac{\xi}{\lambda^2} d\epsilon d\zeta d\lambda \quad (1)$$

where  $f$  is the kinetic distribution function for the exospheric gas,  $g_H$  is the rate of (fluorescent) solar photon scattering per atom, and  $K$  is a constant. The shadow height parameter  $\lambda_1$  indicates the base of the observed column. In this application, explicit consideration of the radial velocity component requires a slight recasting of the dynamical framework used in GS1 and GS2; the momentum is here written in terms of  $\xi$  and  $\zeta$

$$\xi = \frac{p_r}{(2mkT_c)^{1/2}}, \quad \zeta = \frac{p_\chi}{r(2mkT_c)^{1/2}}$$

whereas the radial parameter remains  $\lambda = GMm/kT_c r$ , where  $p_r$  and  $p_\chi$  are the radial and transverse canonical momenta, respectively,  $r$  is the planetocentric distance,  $m$  and  $M$  are the constituent and planetary masses, respectively,  $G$  is the gravitational constant, and  $k$  is the Boltzmann constant. In this application  $\epsilon$  refers to the orientation of the dynamical plane to the magnetic equator.

The integrals in Eqn. (1) are restricted so that only exobase piercing trajectories are populated, while the exopause provides a convenient "ceiling." (The exopause is that radial distance  $r_p$  beyond which the radiation pressure acceleration exceeds the planetary gravitational acceleration.) Writing  $f = f_0 (1 + \Phi)$ , where  $f_0$  denotes the evaporative kinetic distribution along an exobase intersecting trajectory

$$f_0 = \frac{N_c}{\pi^{3/2}} e^{-\psi_c^2}$$

and  $(1 + \phi)$  conveys the effects of solar ionization and resonant charge exchange collisions with plasmaspheric protons, Eqn. (1) becomes

$$4\pi I(\xi, \lambda_1) = \frac{N_c}{\pi^{3/2}} g_H K e^{-\xi^2 - \lambda_c} S(\xi, \lambda_1) \quad (2)$$

$$S(\xi, \lambda_1) = \int_{\lambda_p}^{\lambda_1} \int_{\zeta}^{2\pi} \frac{e^{+\lambda - \zeta^2}}{\lambda^2} \zeta \exp\left[2\alpha\left(\frac{\cos\chi_c}{\lambda_c} - \frac{\cos\chi}{\lambda}\right)\right] \cdot (1 + \phi(\lambda, \chi, \xi, \zeta, \epsilon)) d\epsilon d\zeta d\lambda \quad (3)$$

where  $\chi$  is the solar angle,  $\alpha$  is the (dimensionless) radiation pressure acceleration, and energy conservation along a trajectory has been used to expand  $\psi_c^2$  -

$$\psi_c^2 = \xi^2 + \zeta^2 - \lambda + \lambda_c + 2\alpha\left(\frac{\cos\chi(\lambda)}{\lambda} - \frac{\cos\chi(\lambda_c)}{\lambda_c}\right)$$

$S(\xi, \lambda_1)$  is the spectrum function and contains the information pertaining to deviations from an isothermal gas. In the idealized case evaluated in Chamberlain [1976],  $\alpha$  and  $\phi$  are both zero and the limits on the  $\zeta$ -integral are algebraically determinable. In the applications at hand the proper exobase points of origin for geocoronal atoms are not within algebraic reach ( $\alpha \neq 0$ ), and the inclusion of plasmaspheric charge exchange requires  $(1 + \phi)$  be evaluated step by step along each trajectory sampled by the line of sight (refer to GS2).

The  $\zeta$ -limits are found in these calculations using an iterative search routine of the type employed in GS1 and GS2 to determine related velocity

limits (i.e., the cone of acceptance and minimum escape speed). Figure 1 presents an example of these limits as functions of  $\lambda$  for a specified solar angle ( $\chi$ ) and radial speed ( $\xi$ ). The analytic ( $\alpha = 0$ ) limits of Chamberlain [1976], shown for comparison, are given by ( $\lambda_c$  denotes the exobase level)

$$\begin{aligned}\zeta_{\text{ESC}}^0 &= (\lambda - \xi^2)^{1/2} \\ \zeta_{\text{CONE}}^0 &= \frac{\lambda}{(\lambda_c^2 - \lambda^2)^{1/2}} (\xi^2 + \lambda_c - \lambda)^{1/2}\end{aligned}\tag{4}$$

The computations for  $S(\xi, \lambda_1)$  have been done using the Gaussian net construction employed in GS1 and GS2, modified as appropriate for the current choice of integration variables. The interval  $[\lambda_p, \lambda_1]$  was spanned by 8 or 16 point Gaussian summations, depending on the choice of  $\lambda_1$ , along the solar ( $\chi = 0^\circ$ ) and antisolar ( $\chi = 180^\circ$ ), directions of the Earth-Sun axis; the search routine then determined  $\zeta_{\text{ESC}}(\lambda, \xi)$  and  $\zeta_{\text{CONE}}(\lambda, \xi)$  for each radial summation point and prescribed radial speed. The  $\zeta$ -integrals were then evaluated with 4-point Gaussian summations for each observed component (ballistic, satellite, and escape). These trajectory classes are independent of the orientation between the dynamical plane and the magnetic equator, permitting the  $\epsilon$ -integral to be handled separately. With the dipolar plasmasphere model of GS2, this integral can be restricted to the range  $[0, \pi/2]$  with a multiplicative factor of 4 and was evaluated with a 4-step Simpson arc summation, while with the spherical plasmasphere model this integral simply reduces to a factor of  $2\pi$ . The dependence of the  $\lambda$ - and  $\zeta$ -limits on  $\xi$  is to be emphasized: for  $\xi$  large enough ( $\lambda_c^{1/2}/2$  in the analytic case) there is no satellite contribution, while for  $\xi$  exceeding the shadow height escape speed only the escape component contributes.

### 3. PROFILE EXAMPLES

#### Evaporative Case

Intensity profiles calculated for the simple evaporative case (classical exobase, radiation pressure acting) are displayed in Figure 2, normalized to line center ( $\xi = 0$ ) and evaluated for a variety of shadow heights along a line sight parallel to the midnight axis ( $\chi = 180^\circ$ ). The component contributions to these profiles are also shown. The evaporative satellite component arises from the variation of trajectory angular momentum, induced by radiation pressure, in the manner discussed in GS1. The resulting kinetic distribution is obtained via Liouville's theorem, knowing the exobase density and temperature; at locations well inside the exopause, at bound energies, and for a uniform exobase, it is nearly an isotropic Maxwellian. Thus, while the ballistic component dominates the line near the exobase, this is mostly comprised of tightly bound atoms, and away from the exobase the satellite component makes up most of the observed hydrogen. (Note that a rather cool exobase has been assumed:  $\lambda_c = 6.9$ .) As will be borne out in the ensuing cases, these examples indicate that profile information obtained with shadow heights near or beyond geosynchronous radius applies primarily to the satellite component (or, more properly, the quasi-satellite component). The "gravitational cooling" mentioned by Kerr et al. [1986] is evident here in the increasing narrowness of the profiles as the shadow height is raised.

Comparison with the analytic theory of Chamberlain [1963, 1976] serves to highlight the consequences deriving from radiation pressure dynamics. In the left panel of Figure 3 the midnight axis evaporative (RP,  $180^\circ$ ) intensity profile is shown along with the analytic  $r_{cs} = r_c$  and  $r_{cs} = \infty$  profiles, each normalized to line center, for a shadow height of  $2.50 R_E$ . The variation of profile is not striking in this format, due to the overriding  $\exp[-\xi^2]$  factor.

Removing this factor unveils the true variation among models and permits a fairly uncluttered presentation format. In the right panel of Figure 3 the corresponding spectrum functions are shown, normalized to line center, along with spectrum functions for a line of sight along the noon axis (RP,0°) in the evaporative case and for the analytic  $r_{cs} = 2.50 R_E$  exosphere. The evaporative case spectrum functions exhibit roughly the spectral shape of the analytic  $r_{cs} = \infty$  profile, characterized by a complete Maxwellian bound component; the central minimums generated with finite  $r_{cs}$  values are not present. The narrowness of the  $r_{cs} = \infty$  profile reflects the presence in this model of large numbers of bound atoms at large distances from the planet which necessarily have small radial velocities.

The broadening of the evaporative case profiles relative to the analytic  $r_{cs} = \infty$  profile in Figure 3 is due to the imposition of the exopause by radiation pressure dynamics. High apogee Keplerian orbits are converted by radiation pressure into exopause intersecting trajectories (escape or flyby), resulting in a reduced minimum escape speed ( $\zeta_{ESC}(RP) < \zeta_{ESC}^0$ , refer to Figure 1). In this way, the quasi-satellite component generated by radiation pressure dynamics is curtailed relative to the Keplerian satellite component of the analytic theory. This truncation is more noticeable along the noon axis in that  $\zeta_{ESC}(RP,0^\circ) < \zeta_{ESC}(RP,180^\circ)$  as discussed in GS2, resulting in a slightly broader profile.

Yelle and Roesler [1985] have indicated the plausibility of reformulating the satellite critical radius development to take into account mechanisms acting preferentially on atoms near apogee, of which radiation pressure is the most conspicuous example; Figure 11 of that paper presents an example of the modifications this sort of mechanism might introduce to profiles generated with the analytic theory assuming finite  $r_{cs}$  values. It is a simple matter to

extend the analytic approach of Chamberlain [1976] in this fashion, and it is clear that the exopause concept must play a significant role in this. The idea is to eliminate contributions from atoms, imagined to be executing Keplerian orbits, located outside the exopause. It is not enough, however, to simply subtract trans-exopause contributions from the analytic formulation, as atoms on bound orbits intersecting the exopause would still be counted, i.e., atoms would "magically" disappear on ascending above the exopause only to reappear on descending below. This trick would also emphasize the spectrum function central ( $\xi = 0$ ) minimums and impose such a minimum in the  $r_{cs} \rightarrow \infty$  limit. Rather, the minimum escape speed is modified by taking

$$\zeta_{ESC}^2 = \lambda - \lambda_p - \xi^2 \quad (5)$$

where  $\lambda_p$  is the exopause radial parameter. Within this Keplerian framework, the exopause is simply an altitude ceiling for orbital apogees. When  $r_c < r_{cs} < r_p$ , a limited satellite component is present, while the action of radiation pressure suggests  $r_{cs} = r_p$  to be a credible choice. The determination of component contributions parallels the earlier analytic development, with  $\zeta_{CONE}$  retaining the form given in Eqns. (4). A satellite component contribution to the intensity profile exists when  $r_{cs} > r_c$  and

$$\xi^2 < \frac{\lambda_c^2}{4(\lambda_c - \lambda_p)} - \lambda_p \quad (6)$$

Figure 4 displays the success of this simple extension of the analytic approach by comparing the evaporative (RP) profiles with profiles generated with this revised analytic theory. In view of the calculational effort required to handle radiation pressure dynamics, this simple, intelligible

model may prove useful as an interpretational aid in the analysis of observed spectral line profiles.

(The central minimums of the spectrum functions generated with finite  $r_{cs}$  values in the analytic development of Chamberlain [1976], and the associated broad profiles, might lead to misinterpretations of line profiles. Yelle and Roesler [1985] concluded that the narrow profiles observed near midnight could not be matched to analytic models with large  $r_{cs}$  values, contrary to the results shown in Figure 3 (see also Figure 1 of Chamberlain [1976]). Of the analytic models, the only reproduction of narrow lines is obtained when  $\lambda_{cs} \rightarrow 0$  ( $r_{cs} \rightarrow \infty$ ), in which the central minimum exhibited by spectrum functions with finite  $r_{cs}$  values becomes too narrow to appear. It must be acknowledged, of course, that this similarity of profile shape is to some extent fortuitous, in that the limit  $\lambda_{cs} \rightarrow 0$  is clearly unrealistic. However, as  $r_{cs}$  values increase with other exospheric parameters remaining constant, the exospheric content increases, which would yield better agreement with the line-integrated intensity measurements reported by Yelle and Roesler. As a separate note, the velocity or phase space regions corresponding to the kinetic trajectory classes (ballistic, satellite, and escape) are independent of the exobase temperature, and are determined solely by gravity in these analytic models.)

### Solar Ionization

Solar ionization is treated in this work as a simple exponential decay (refer to GS1, Eqn. (12), and GS2, Eqn. (15)). Spectrum functions illustrating the modified spectral shapes resulting from solar ionization are displayed in the upper two panels of Figure 5 for shadow heights of  $2.50 R_E$

and  $6.632 R_E$  (geosynchronous radius) and look direction along the midnight axis. The bound component contributions are also shown. Normalization is with respect to the center of the evaporative spectrum function. The line profiles overall appear broader due to the relative weakening of the line center, reflecting the preferential loss of satellite atoms. The ballistic component contribution shows an expected slight depletion on the blueward or descending motion wing, due to the longer exposure of post-apogee ballistic atoms to solar ionizing emissions. The satellite component redward (ascending motion) depletion is an unexpected feature and is strong enough to give the entire line an apparent blue shift that is only offset by the appearance in the redward wing of the escape component contribution, which graphs as a "ledge" in this format. This blueward biasing near line center indicates that at altitudes removed from the exobase ( $r > 2.00 R_E$ ), satellite atoms with radial velocity components toward the planet when intersecting the midnight axis have average flight times shorter than those traversing the same satellite trajectories in the reverse sense.

Figure 5 also displays the corresponding noon axis spectrum functions in the lower two panels (for which the idea of a shadow height is artificial). The ballistic and escape component contributions are similar to those along the midnight axis, with the line as a whole being wider and the ballistic component providing a greater part of the intensity, consequences of the imposition of an exopause by radiation pressure dynamics as discussed earlier. The satellite component is again striking, exhibiting an effective "age" difference between ascending and descending motions in a manner reversed to the biasing along the midnight axis and imparting an unmistakeable redward shift in these profiles.

This distinction between motion components toward and away from the

exobase along trajectory segments that do not directly intersect the exobase can only be attributed to radiation pressure dynamics. It is, however, difficult to gain insight into the dynamical underpinning of this phenomenon, partly because the spherical description of velocity space is not "natural" to the geometry of the situation. Rather, the theoretical framework used here and set forth in GS1 and GS2 has been constructed to allow a direct identification of the osculating satellite population for comparison with earlier work. Only two evaporative components, bound and escaping, to the exospheric population are physically well defined, with the demarcation between ballistic and satellite trajectories being somewhat artificial; the distinction is simply that a satellite trajectory loops the planet a finite number of times between exobase intersections (with evolving orbital parameters) and is properly looked upon as ballistic before its first and after its last apogee. This behavior was first outlined in Chamberlain [1979], where a perturbation treatment of the dynamical effects of radiation pressure was used to demonstrate that tightly bound satellite orbits eventually crash into the planet. However, fluorescent scattering by the tightly bound atoms encompassed within that treatment must contribute symmetrically about the line center whether time-of-flight loss mechanisms are operating or not. Thus the biasing exhibited in Figure 5 must reflect the evolutionary patterns of satellite orbits not tightly bound, although just how to isolate this higher speed component is not immediately apparent.

#### Plasmasphere Interaction

Spectrum functions obtained with the geocoronal model interacting with the spherical plasmasphere model of GS1 and GS2, presented in the upper two panels of Figure 6, are reminiscent of those incorporating solar ionization.

The shadow heights in this figure are  $2.50 R_E$  and  $6.632 R_E$  with look direction along the midnight axis, and the bound component contributions are again displayed. The erosion of the bound population by charge exchange collisions with the too hot, too dense spherical plasmasphere model weakens the center of the line considerably and is complemented by the generation of a strongly enhanced escape component. Again, the distinction between blueward and redward satellite contributions is indicative of a longer exposure to the plasmasphere of satellite atoms on the nightside moving away from the planet, resulting from the satellite orbit evolution caused by radiation pressure dynamics.

The lower two panels of Figure 6 illustrate the effect of interaction with the dipolar plasmasphere model of GS2. The dipolar plasmasphere generates an overall increase in line intensity, most of which is due to a strongly enhanced satellite component. An enhancement of the escape component contribution is also present, though it is not as prominent a feature as when the spherical plasmasphere model is employed. In these applications, geocoronal kinetic modifications resulting from the plasmasphere interaction are mainly determined by the plasma temperature profile. The dipolar shape of the plasmopause is not an important consideration for axial orientations. The temperature profile used in these calculations and in GS2, taken from Chiu et al. [1979], increases quickly from 2000K near the exobase to 5000K. The main effect of the interaction in this instance is to convert low energy neutrals, which are quickly replenished, into higher speed atoms that attain to outer geocoronal locations while still remaining bound. Thus, with the dipolar plasmasphere model, which is somewhat realistic though steady state, charge exchange regenerates the satellite component kinetic distribution, leading to both enhanced column densities and a partial erasing of the "age" biasing.

Note that with the selected shadow heights ( $r > 2.00 R_E$ ), no appreciable downward escape component contribution is evident, nor is one to be expected.

### Geocoronal Profiles

It is clear from the above examples that radiation pressure, superimposed on the planetary gravitational acceleration, controls the general form of optically thin profiles, although the distortions caused by solar ionization and plasmaspheric charge exchange collisions can be considerable. In particular, narrow line widths such as those displayed by the examples of Figure 2 should be looked upon as being typical, reflecting the extensive quasi-satellite component sustained by radiation pressure. Broader geocoronal lines would then correspond to a relative weakening of emission at line center caused by a depletion of satellite atoms, and would most likely be associated with periods of high solar activity (i.e., strong ionizing fluxes) or high topside ionospheric temperatures or both. A blueward intensity biasing near line center, for lines of sight parallel to the antisolar axis, can be expected when such conditions persist. These modifications, though, are embellishments, imposed by population mechanisms, to a profile narrowness established by radiation pressure dynamics.

An interesting aid to profile analysis follows from this assessment. As noted above, the escape component emission graphs as a "ledge" in the spectrum function format, and in fact merges with the bound component emission at a fairly fixed spectral displacement (approximately given by the right-hand side of inequality (6)). This "merging point" is obviously not a temperature-related feature; rather, it indicates the spectral displacement at which the escape component begins to dominate the line and so is determined by dynamics. It is suggested that this point may provide the most useful

reference displacement for defining the spectral line width in exospheric situations. It can also be used to gauge whether the bound component emission is depleted or enhanced relative to evaporative levels, in that the value of the spectrum function at this point has varied little as the various examples have been considered. Even with the spherical plasmasphere model, the merging point remains close to its evaporative location in Figure 6.

The line profiles along the midnight look direction for both plasmasphere interaction models, normalized to the respective line centers, are shown in Figure 7. These incorporate solar ionization in the manner described in GS2. For purposes of comparison to observations, these profiles can be considered to be "realistic". It can be anticipated that quiet conditions must persist for several days for the exosphere to approach the steady state configuration assumed in the calculations reported here and in GS2. In view of the similarity between the dipolar plasmasphere interaction and simple evaporative profiles, the slight blueward line center biasing and the slight enhancement of the escape wing in the former are not easily perceived in this format.

#### 4. IMPLICATIONS FOR $H_{\alpha}$ PROFILE MEASUREMENTS

Measurements of the geocoronal  $H_{\alpha}$  line profile have been independently carried out and reported by Yelle and Roesler [1985] and Kerr et al. [1986]. Yelle and Roesler restrict themselves to a limited set of observations with maximum shadow heights of roughly two Earth radii and look directions in the antisolar direction; the emphasis of their paper is on comparison with the analytic theory of Chamberlain [1976] and the Monte-Carlo results of Hodges et al. [1981] and on assessing profile modifications introduced by eliminating

atoms with high altitude apogees. On the basis of their Figure 11, Yelle and Roesler suggested that ground based observations of narrow  $H_{\alpha}$  profiles may indeed be attributable to a depletion of atoms moving along highly eccentric orbits.

Kerr et al. [1986] provide a much more extensive set of observations pertaining to several lines of inquiry; local time variations in exobase temperature and column densities are discussed in addition to the presentation of line profiles. Kerr et al. make a strong case for the important influence of  $H^+$  fluxes on exobase temperatures and the resultant exospheric content. In particular, Kerr et al. [1986] appear to have directly observed the early morning hydrogen trough [Vidal-Madjar and Thomas, 1978]. The observations contained in Kerr et al. [1986], made at Arecibo with zenith lines of sight, encompass profile measurements with large shadow heights in the antisolar direction, thus complementing the coverage of Yelle and Roesler. However, Yelle and Roesler and Kerr et al. each relied on differing interferometer set-ups and deconvolution techniques, making it difficult to directly compare the profiles obtained by the two groups.

The narrow profiles retrieved by Yelle and Roesler seem to concur with the expectations of this paper. Interestingly, Yelle and Roesler note a slight blue shift to the observed emission profiles, though the measurements were not of sufficient quality to quantitatively fix this. On the basis of the calculations summarized in Figures 5-7, and contrary to earlier notions, the satellite component is to be considered responsible for this blueward biasing. This implies in turn that in the Fabre-Perot interferometer deconvolution procedures, care should be exercised not to automatically take the profile peak to coincide with the stationary line center.

Anomalously broad midnight profiles were sometimes recorded by both

groups. In fact, Kerr et al. obtained only a few examples of narrow midnight profiles. Magnetic disturbances or simply nonquiet conditions were mentioned in each paper as perhaps having some direct influence on these anomalies. It is likely that multiple scattering contamination from near-exobase or upper thermospheric altitudes contributes to some extent. The large shadow heights and resultant low intensities involved in the Kerr et al. measurements are particularly susceptible to shadow region contamination. In the absence of a recognized auxiliary excitation mechanism, multiple scattering of solar Lyman- $\beta$  seems to be the only way to account for the conspicuous emissions often seen in their data at spectral displacements on the blue wing exceeding that defined by the shadow height escape speed for shadow heights above the plasma-pause. Since most geocoronal modifications brought about by charge exchange are effected by collisions at altitudes inside  $2.00 R_E$ , any profile perturbations induced by  $H^+$  fluxes near the exobase would not be directly observable for shadow heights above this zone. Of course, these fluxes would affect profiles indirectly, by perturbing exobase conditions [Kerr et al., 1986] and possibly by influencing multiple scattering contamination.

The theoretical profiles presented in Figure 7 (applicable to conditions approaching steady state, with quiet magnetic conditions persisting for several days prior to observation and for low to moderate solar activity epochs) might be useful in attempts to gauge the extent of multiple scattering contamination, when compared with the near midnight profiles measured by Kerr et al., for instance. Actually, a firmer handle on multiply scattered Lyman- $\beta$  contamination is not difficult to gain since the geocoronal  $H_\alpha$  signal is not itself scattered. The proposed technique for isolating this contamination involves the "merging point" which appears in the spectrum function format. Obviously, this is a viable reference point only if shadow region

contamination is negligible or removable. Note, though, that the emission profile from a layer of gas characterized by a Maxwellian kinetic distribution (i.e., possessing an isotropic temperature  $T_g$ ) graphs in this format as

$$C \exp\left[-\frac{P_r^2}{2mk} \left(\frac{1}{T_g} - \frac{1}{T_c}\right)\right]$$

where  $C < 1$  is a normalization factor. Thus,  $H_\alpha$  originating from upper thermospheric altitudes ought to be characterized by a nearly flat spectrum function ( $T_g = T_c$ ). A contribution of this sort to an observed geocoronal profile would be easily recognized on the blue wing, particularly for shadow heights above  $2.00 R_E$  where no appreciable charge exchange generated capture component is expected. In brief, multiple scattering contamination should appear as a smoothly varying, recognizable background in the spectrum function format, superimposed on the single-scattering emission and hence removable.

The bearing of the Monte Carlo simulations of Tinsley and colleagues [Hodges, et al., 1981; Tinsley et al., 1986] is not easily assessed. Both Yelle and Roesler [1985] and Kerr et al. [1986] cite the event statistics presented in Hodges et al. [1981] but are only able to infer tentative conclusions regarding the interpretation of line profile measurements. Nor are the consequences stemming from the evolution of satellite atom orbits consistently taken into account in these studies. Yelle and Roesler constructed a geocoronal line profile (shadow height 13760 km, planetocentric distance) from the radial velocity distribution functions described in Hodges et al. [1981] (hot  $H^+$  model, midnight averages) which exhibits a blueward displacement of the emission peak. Inspection of the midnight radial velocity distributions given by Tinsley et al. [1986, Figure 7] has turned up another apparent example of a net blueward shift, for shadow heights between 13300 km

and  $\sim 40000$  km (planetocentric distances). These extrapolations are not conclusive, however. In both sets of simulations, the significance of statistical errors is not made clear, nor is much gained by way of interpretive insight. Indeed, the only modification to zenith line profiles that can be firmly predicted on the basis of these simulations (or earlier work, for that matter) is an enhancement of the escape and capture component contributions by plasmaspheric charge exchange collisions.

$H_{\alpha}$  profile measurements constitute a promising technique for studying the geocorona. Undoubtedly, it is a simpler matter to analyze observations of this type than the earlier absorption cell studies of Lyman- $\alpha$  line profiles, which are notoriously difficult to interpret [Bertaux, 1978; Prisco and Chamberlain, 1979]. A number of points remain to be resolved, however, before a comprehensive interpretive framework for geocoronal  $H_{\alpha}$  measurements can be advanced. Nevertheless, narrow  $H_{\alpha}$  profiles can no longer be considered "anomalous." It is also evident that the extent of the satellite atom population is disclosed in the analysis of pure geocoronal profiles; the spectrum function format should prove very useful in facilitating profile analysis. Among the unresolved points, the question of the influence of  $H^{+}$  fluxes cannot be addressed at this time, due to the low shadow heights near the terminator required to directly investigate possible spectral signatures of these fluxes; in particular the confinement to axial orientations must be relaxed to properly predict line features for observations made near the terminator. Also, nonuniform exobase density and temperature variations are likely to play a dominant role in profile formation at shadow heights below  $2.00 R_E$ , and the adoption of a standard exobase model is not a straightforward procedure [Vidal-Madjar and Thomas, 1978]. For these reasons theoretical profiles have not been presented for near-exobase shadow heights. The

satellite trajectories participating in the blueward biasing of emissions along the midnight axis need to be isolated and the orbital evolution clarified. Fine structure distortions may play a significant role, perhaps in conjunction with an auxiliary excitation mechanism. This last question has been pursued separately [Chamberlain, unpublished manuscript].

#### ACKNOWLEDGMENTS

This research was sponsored by the Atmospheric Research Section, National Science Foundation, under grant ATM-8415118, and by the National Aeronautics and Space Administration under grant NSG-7043, both to Rice University.

## REFERENCES

- Bertaux, J. L., Interpretation ofOGO-5 line shape measurements of Lyman-alpha emission from terrestrial exospheric hydrogen, Planet. Space Sci., 26, 431-447, 1978.
- Bishop, J., Geocoronal structure: The effects of solar radiation pressure and the plasmasphere interaction, J. Geophys. Res., 90, 5235-5245, 1985.
- Bishop, J., and J. W. Chamberlain, Geocoronal structure 2, Inclusion of a magnetic dipolar plasmasphere, submitted to J. Geophys. Res., 1986.
- Chamberlain, J. W., Planetary coronae and atmospheric evaporation, Planet. Space Sci., 11, 901-960, 1963.
- Chamberlain, J. W., Spectral line profiles for a planetary corona, J. Geophys. Res., 81, 1774-1776, 1976.
- Chamberlain, J. W., Depletion of satellite atoms in a collisionless exosphere by radiation pressure, Icarus, 39, 286-294, 1979.
- Chiu, Y. T., J. G. Luhman, B. K. Ching, and D. J. Boucher, Jr., An equilibrium model of plasmaspheric composition and density, J. Geophys. Res., 84, 909-916, 1979.
- Hodges, R. R., R. P. Rohrbaugh, and B. A. Tinsley, The effect of the charge exchange source on the velocity and 'temperature' distributions and their anisotropies in the Earth's exosphere, J. Geophys. Res., 86, 6917-6925, 1981.
- Kerr, R. B., S. K. Atreya, J. W. Meriwether, Jr., C. A. Tepley, and R. G. Burnside, Simultaneous  $H_{\alpha}$  line profile and radar measurements at Arecibo, J. Geophys. Res., 91, 4491-4512, 1986.
- Prisco, R. A., and J. W. Chamberlain, Doppler line profiles in a planetary corona: An extended approach, J. Geophys. Res., 84, 4363-4370, 1979.

Tinsley, B. A., R. R. Hodges, Jr., and R. P. Rohrbaugh, Monte-Carlo models for the terrestrial exosphere over a solar cycle, J. Geophys. Res., in press, 1986.

Vidal-Madjar, A., and G. E. Thomas, The terrestrial hydrogen problem, Planet. Space Sci., 26, 863-871, 1978.

Yelle, R. V., and F. L. Roesler, Geocoronal Balmer alpha line profiles and implications for the exosphere, J. Geophys. Res., 90, 7568-7580, 1985.

## FIGURE CAPTIONS

Figure 1. Spectrum function integration limits for specified  $\chi$  and  $\xi$  when radiation pressure (RP) acts. Integration over  $\lambda$  extends from the exopause ( $\lambda_p = 0.2056$ ) to the desired shadow height  $\lambda_1$ . Integration over  $\zeta$  is broken into intervals corresponding to ballistic ( $0 \leq \zeta \leq \zeta_{\text{CONE}}$ ), satellite ( $\zeta_{\text{CONE}} < \zeta < \zeta_{\text{ESC}}$ ), and escape ( $\zeta_{\text{ESC}} \leq \zeta$ ) components. When  $\zeta_{\text{ESC}} < \zeta_{\text{CONE}}$  everywhere, no satellite component is possible. Dashed curves correspond to the analytic theory limits ( $\alpha = 0$ ) given by Eqns. (4). The  $\zeta$ -limits are squared in this figure to simplify the appearance.

Figure 2. Evaporative case (exobase source, radiation pressure acting) line profiles for look directions along the midnight axis ( $\chi = 180^\circ$ ) for a variety of shadow heights (given as planetocentric distances, with the exobase placed at 6871 km). Profiles are normalized to line center. Component contributions to the respective profiles are also shown. In these calculations, the exobase temperature  $T_c$  has been set to 1020K and the radiation pressure acceleration taken to be  $0.75 \text{ cm/sec}^2$ . Accordingly, the reference speed is  $(2kT_c/m)^{1/2} = 4.123 \times 10^5 \text{ cm/sec}$  and the exopause  $r_p$  has been placed at a planetocentric distance of  $36.20 R_E$ . The shadow height escape speeds of the revised analytic theory are given below the shadow height ( $\psi_{\text{ESC}}(\lambda_1) = (\lambda_1 - \lambda_p)^{1/2}$ ). The bound component contributions are bracketted by this speed in each instance.

Figure 3. Comparison of evaporative case line profiles with analytic model results for a shadow height of  $2.50 R_E$  ( $T_c = 1020\text{K}$ ). Left panel: shown are analytic model profiles (characterized by extreme satellite critical radius values) along with the midnight axis evaporative (RP,  $180^\circ$ ) profile, each

normalized to line center. Right panel: spectrum functions for the cases illustrated in the left panel, along with the noon axis evaporative (RP,0°) and analytic  $r_{cs} = 2.50 R_E$  spectrum functions, each normalized to line center.

Figure 4. Comparison of the evaporative noon (RP,0°) and midnight (RP,180°) profiles with revised analytic model profiles incorporating an exopause  $\lambda_p$  (refer to Eqn. (5)), for a shadow height of  $2.50 R_E$ . Format is the same as in Figure 3.

Figure 5. Effect of solar ionization. Spectrum functions for emissions along midnight and noon axes (shadow heights of  $2.50 R_E$  and  $6.632 R_E$ ) are shown for the solar ionization (solid curve in each panel) and the simple evaporative (dashed curve) cases. Normalization is with respect to the center of the evaporative case curve to illustrate the spectral variation resulting from ionization loss. The bound component contributions for the solar ionization case are also displayed. Note that the escape "ledge" alone contributes above the shadow height escape speed. (Assumed solar ionization decay time:  $T_{sol} = 10$  days.) Not shown: exobase shadow height spectrum functions exhibit the same sort of biasing, although to a less conspicuous degree due to the intrinsic width of near-exobase profiles and the dominance of the ballistic component there. Biasing of profiles persists to shadow heights of  $10.00 R_E$ , but at that column base distance the spectrum functions and corresponding satellite contributions exhibit a lesser degree of asymmetry near line center, indicating a reduction of the implied effective satellite "age" difference.

Figure 6. Effect of the plasmasphere interaction. Spectrum functions for emissions along the midnight axis for  $2.50 R_E$  and  $6.632 R_E$  shadow heights are shown for geocoronal models incorporating charge exchange collisions with the plasmasphere models of GS2 (solid curve in each panel). Bound component contributions to the plasmasphere interaction cases are also shown, and normalization is with respect to the center of the simple evaporative profile (dashed curve). The weakening of the bound population emission in the interaction with the too hot, too dense spherical plasmasphere is dramatic and is in sharp contrast to the line center enhancement resulting in the dipolar plasmasphere interaction. (The spherical plasmasphere model is characterized by an isothermal, diffusive equilibrium  $H^+$  density distribution with a spherical plasmopause at geosynchronous radius. The dipolar plasmasphere model is that of Chiu, et al. [1979] evaluated for low-to-moderate solar activity conditions. The parameter values chosen for the calculations are given in GS2, Table 1.)

Figure 7. Line profiles for look direction along the midnight axis for  $2.50 R_E$  and  $6.632 R_E$  shadow heights. Normalization is with respect to the individual line centers. Solar ionization has been included in conjunction with interaction with the indicated plasmasphere models; the simple evaporative case profile is also shown (dashed curve).

FIG. 1

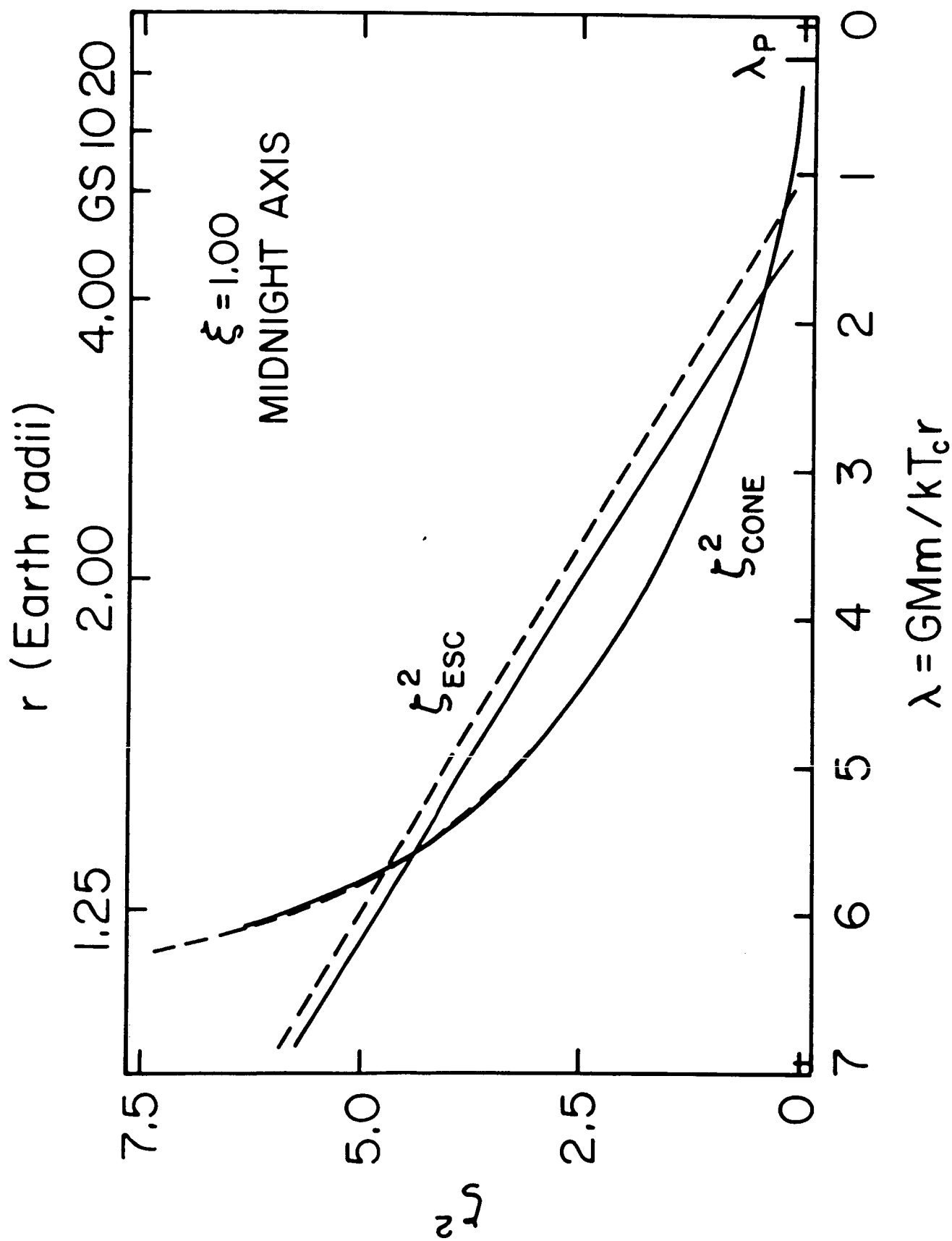


FIG. 2

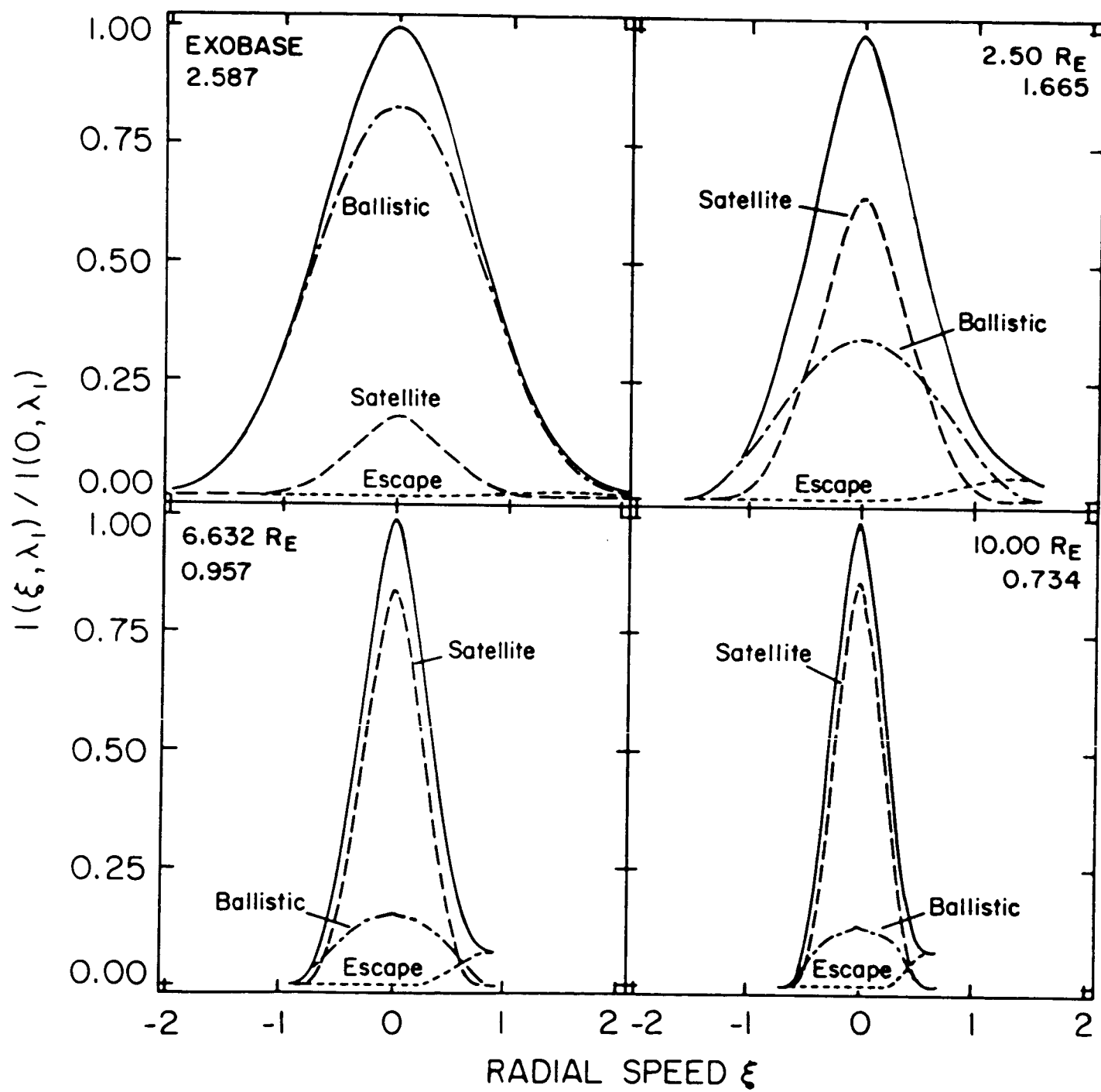


FIG. 3

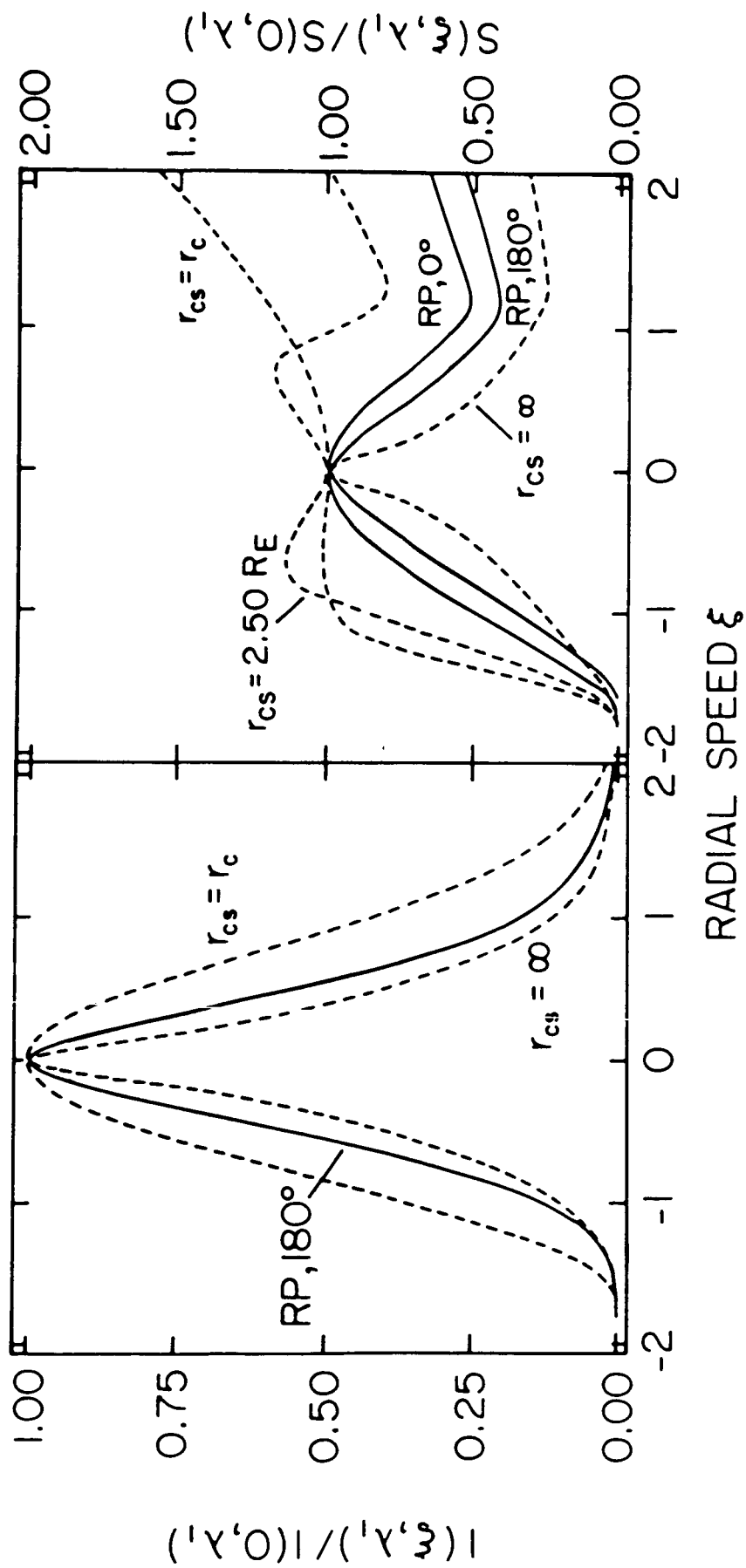


FIG. 4

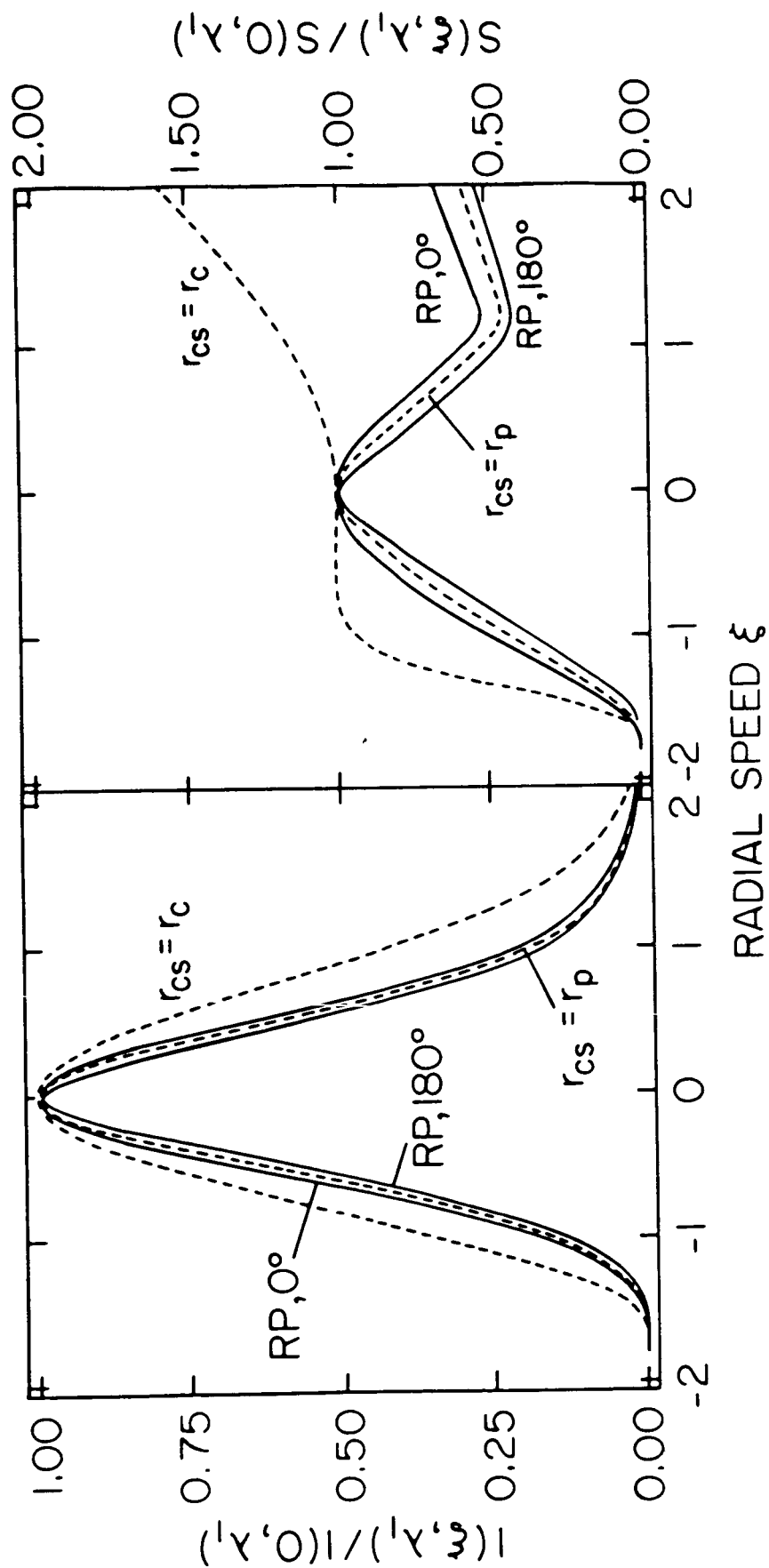


FIG. 5

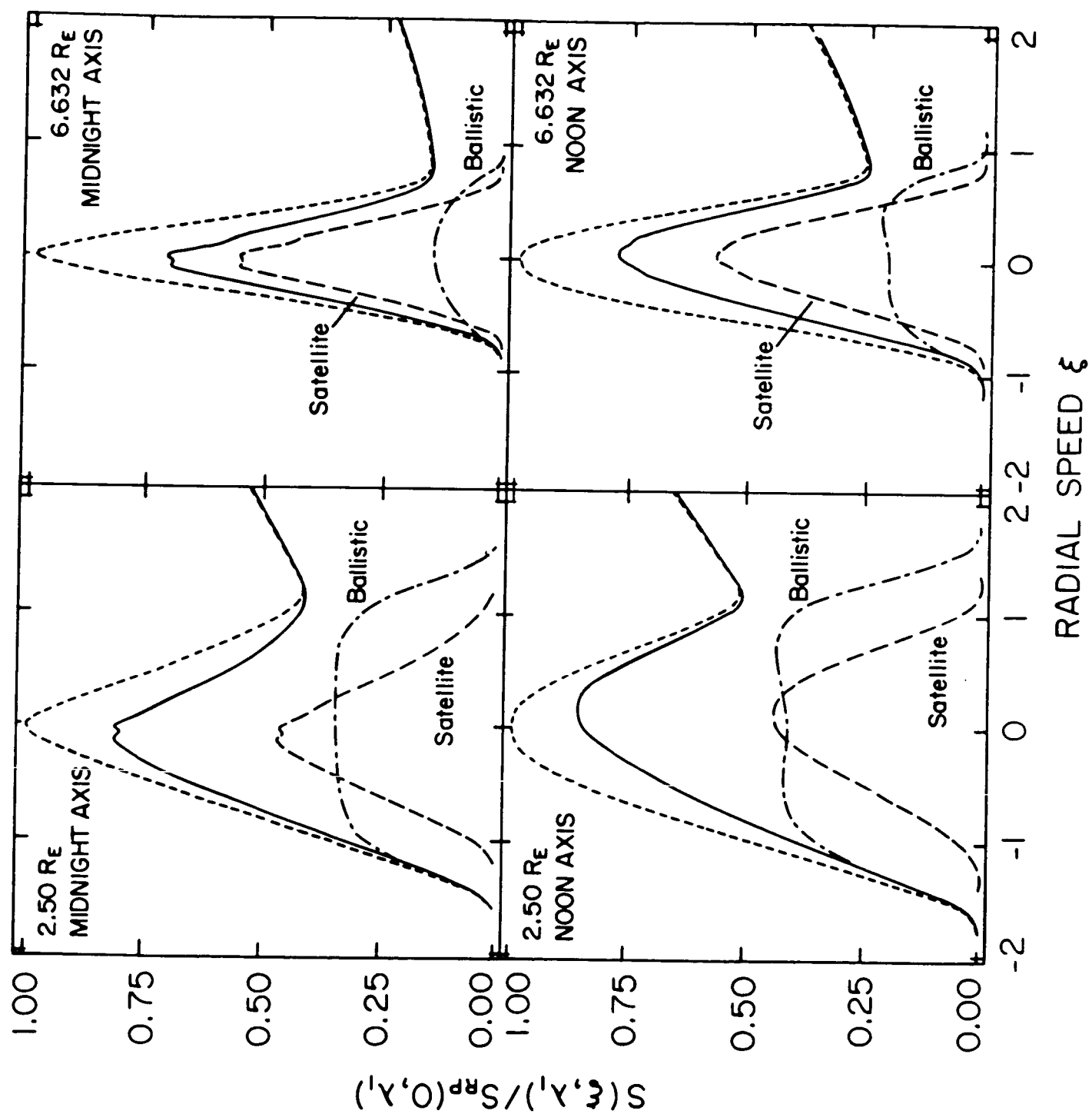


FIG. 6

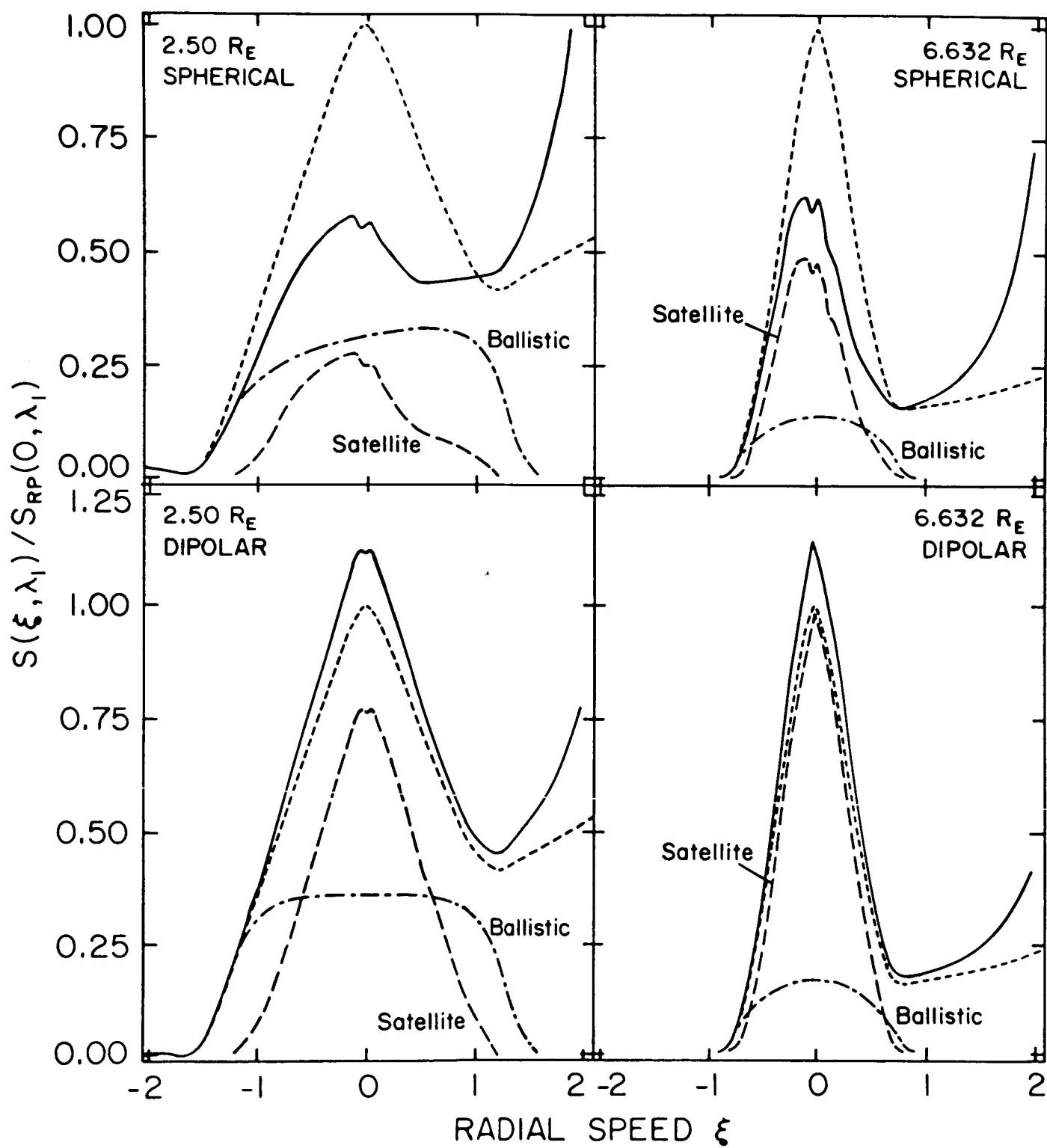


FIG. 7

